IEEE Access
Multidisciplinary | Rapid Review | Open Access Journal

Received August 28, 2019, accepted September 19, 2019, date of publication September 23, 2019, date of current version October 4, 2019.

Digital Object Identifier 10.1109/ACCESS.2019.2943248

Structured Light-Based Visual Servoing for Robotic Pipe Welding Pose Optimization

JINQUAN LI[1], ZHE CHEN[1,2], GANG RAO[2], AND JING XU[2], (Member, IEEE)
[1]School of Automation, Beijing University of Posts and Telecommunications, Beijing 100876, China
[2]State Key Laboratory of Tribology, Department of Mechanical Engineering, Tsinghua University, Beijing 100084, China

Corresponding author: Jing Xu (jingxu@tsinghua.edu.cn)

This work was supported in part by the National Key Research and Development Program of China under Grant 2017YFC0822204, in part by the National Natural Science Foundation of China (NSFC) under Grant U1613205 and Grant 51675291, and in part by the State Key Laboratory of China under Grant SKLT2018C04.

ABSTRACT In order to optimize the pose of welding torch preplanned by offline programming, a structured light-based visual servoing method is proposed. First of all, a series of phase shifting patterns are projected to acquire the so-called phase map. Afterwards, unlike usual feature extraction methods, which were based on 3-D cloud, a cylinder axis is extracted directly from the phase map to represent the connecting pipes' cylindrical surface. Then, a visual servoing control law based on the axis combined with the seam center in phase map is proposed to optimize the pose of the welding torch. Moreover, global asymptotic stability of this method is proved. Finally, simulations and real experiments are performed to demonstrate the effectiveness and robustness of this method. Results show this method can improve the mean error of deviated distance and angle of offline programming by 73.5% and 82.5%, respectively.

INDEX TERMS Robotic welding, structured light, feature extraction, robotic positioning, visual servoing, offline programming.

I. INTRODUCTION

Pipe welding is one of the most reliable and prevalent methods for pipe connection [1]. Compared with manual pipe welding, automatic pipe welding has been increasingly used because of its high safety, quality, productivity and low cost [2]–[4]. In automatic pipe welding techniques, carriage and band system-based mechanized gas metal arc welding (GMAW) is dominant, which ensures the welding quality by laying a band on the pipe surface so that the welding carriage that holds the welding torch can rotate around the pipe [2]. To promote productivity and reliability, a dual-tandem welding process was designed, consisting of two welding torches, with each torch having two wires, and a seam tracking algorithm was proposed based on an arc sensor [3]. However, installing and removing the band and the welding carriage are time consuming.

To improve the productivity and flexibility, robotic pipe welding was studied. A five-axis welding manipulator for GMAW of steel pipe was designed, and seam tracking and weld pool control based on a vision sensor was realized [4]. A robotic system was developed in welding pipes for desalination of sea water [5]. However, the position and orientation (pose) of the welding torch with respect to (w.r.t) the welding joint of the pipe was manually set, and only the torch-to-seam center deviation was eliminated online, an approach that can cause bad welding quality.

Currently, most welding robots still work in the ''teach and playback'' mode [6]. To eliminate the errors that occur during installation of a workpiece and manual teaching itself, online adjustments, such as seam tracking or weld pool control, were widely studied [7]–[10]. However, the ''teach and playback'' mode combined with an online adjustment is not suitable for robotic pipe welding for two reasons. First, compared with a straight line, forming a smooth circular path requires teaching of too many path points, which takes considerable time. Second, in pipe welding, not only does the deviation between the torch tip and the seam center need to be eliminated, but also, the torch needs to point directly at the axis of the pipe, with a certain constant distance, to obtain superior welding quality [11]–[13]; that is, both the position and the orientation of the welding torch must be optimized.

Compared with the ''teach and playback'' mode, offline programming is a promising technique that plans the robotic

The associate editor coordinating the review of this manuscript and approving it for publication was Jinguo Liu.

path based on the model of workpiece [14]–[17]. However, it has two disadvantages: first, installation and modeling errors and robot and part deformation will affect its accuracy. Second, welding robots with a high absolute positioning accuracy are required, as each path point is represented; however, this positioning accuracy is usually lower than the repeatable positioning accuracy for welding robots [16]. To address these issues, some researchers reconstruct the workpiece and workplace using 3-D sensors, based on which the path of torch is planned. Yang *et al.* utilized a stereo structured light sensor to reconstruct the 3D point cloud of workpiece, extracted the weld seam and further plan the 3-D path for welding robot [18]. Maiolino *et al.* integrated ABB's proprietary offline programming system RobotStudio with a structured light based RGB-D sensor to facilitate the automation of sealant dispensing [19]. These methods enabled the ability to dynamically adapt the model, thus coping with environmental and parts variability. However, constrained by calibration errors and reconstruction noise, accuracy is not very desirable.

To improve the accuracy of offline programming, the welding torch needs to be optimized at each path point. For this purpose, visual servoing is a promising method that utilizes visual features to realize robot motion control [20], [21]. According to the designed visual feature, visual servoing can be divided into three categories: image based visual servoing (IBVS) [22], [23], in which visual features defined in 2D image space are directly used to control the robot; position based visual servoing (PBVS) [24], in which visual features are used to estimate the pose of the object coordinate frame w.r.t the camera coordinate frame in 3D Cartesian space and the pose is further used to control robot; and hybrid visual servoing [25], [26], which combines IBVS and PBVS. The accuracy and robustness of visual servoing depend on the visual feature extraction. However, in many industrial applications, objects are texture-less, which means that visual features can barely be extracted by traditional passive vision.

To provide robust visual features for texture-less objects, laser pointers were utilized to facilitate visual servoing [27], [28]. Four parallel laser pointers were utilized to form four feature points on a texture-less plane, and the IBVS control law based on the four points was synthesized to perform a classical plane-to-plane task [27]. One laser pointer was used to provide an extra feature point on a plane object and further estimate the depth to obtain the interaction matrix of IBVS in real time in [28]. However, the laser pointer-based visual servoing approach has two limitations. First, it cannot provide a dense surface profile of a curved surface, so it is difficult to realize a visual servoing task on a complex-shaped object. Second, it is not robust because laser points may leave the camera's field of view, further leads to failure in visual servoing. To this end, structured light methods were introduced to aid visual servoing because it can provide an accurate and dense surface profile of texture-less objects [29]–[33]. In [29], depth difference in phase map is utilized to extract the contour of object, on which visual features are established for achieving robotic translational positioning task. Xu et al. directly utilizes every entry of phase map as visual feature, which can handle positioning task with respect to free-form surface profile theoretically, but only relatively small convergence area is ensured [30]. Structured light-based visual servoing was studied to perform a plane-to-plane task for robotic spraying [31]. In this method, a dense phase map is utilized to design visual features to ensure robustness to noise. However, only a plane-to-plane positioning task was considered, so it is difficult to apply the approach to a cylindrical pipe.

To the best of our knowledge, visual servoing for a texture-less cylindrical surface is still missing from the market and the literature. Motivated by these facts, we developed a structured light-based visual servoing method to optimize the pose of the welding torch at preplanned path points for pipe welding. The benefits of structured light-based visual servoing method are twofold. First, it can deal with those tricky cases when the object is texture-less, even without contour. Second, structured light-based visual servoing can combine structured light method's high-accuracy measurement with visual servoing's robust control, thus achieving high-accuracy positioning. We choose such a method exactly out of these two reasons. The goal of this paper is to optimize the pose of welding torch with respect to steel pipes, so accurate and dense surface information of steel pipes must be acquired. But the surface of steel pipes is texture-less, which means structured light method is a suitable way to acquire accurate and dense surface profile of steel pipes. Second, the goal of our robotic task is to achieve high positioning accuracy, so structure light-based visual servoing can suit our needs.

In this method, phase shifting patterns are projected onto the texture-less pipes to obtain a phase map, a two-dimensional matrix which implicitly contains three-dimensional information. Then, a low-dimensional cylindrical axis is directly extracted from the phase map to represent the cylindrical surface, and the seam center is also extracted to represent the axial position of the weld seam, expediting control. Then, a visual servoing control law based on the extracted cylindrical axis and seam center is proposed for robot positioning, which optimizes the pose of the welding torch at each preplanned path point for robot welding. This method focuses on optimizing the orientation of welding torch, torch-to-tip deviation and nozzle-to-work distance at the same time while most of the present investigations related to robotic welding only focus on the latter two, online or offline.

The main contributions of this paper are as follows:

First, a method for low-dimensional cylindrical axis extraction directly from a high-dimensional phase map is proposed.

Second, an image-based visual servoing (IBVS) control law based on extracted features is designed, and the global asymptotic stability of the control law is proved.

The remainder of this paper is organized as follows. The fundamentals of the structured light-based visual servoing method are presented and analyzed in section II.

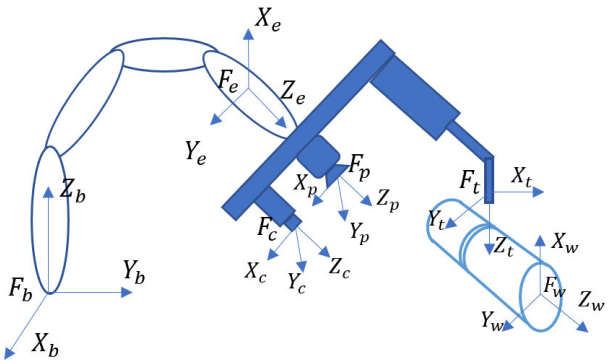

FIGURE 1. Coordinate frames of the system.

The extraction of features representing two connecting pipes is illustrated in III. The deduction and stability analysis of the control law are described in section IV. Simulation experiments and real experiments are performed to verify this method in section V and section VI, respectively. Finally, conclusions are drawn in section VII.

II. FUNDAMENTALS OF STRUCTURED LIGHT-BASED VISUAL SERVOING

In this section, first, the configuration of the structured light-based robotic welding system is described. Second, robotic task is presented. Third, the principle of structured light-based visual servoing by using a phase map is illustrated. Finally, the definition and generation of the phase map are given.

A. DESCRIPTION OF THE SYSTEM

The structured light-based robotic welding system consists of a six-axis robot, a camera, a projector, and a welding torch, together with a welding machine. The camera, projector, and welding torch are all fixed on the robot end effector, so the relative pose between each of them remains constant. For notation consistency, the coordinate frames of this system are denoted as follows. As shown in Fig.1, the camera frame is denoted with F_c, the projector frame is denoted with F_p, the robot base frame is denoted with F_b, the end effector frame is denoted with F_e, the torch frame is denoted with F_t, and the pipe frame is denoted with F_w, where axis Z_w coincides with the central axis of the cylindrical pipe. ${}^aT_b$ represents the transformation matrix of frame a w.r.t frame b.

B. DESCRIPTION OF THE ROBOTIC TASK

The robotic task is to position the welding torch at each pre-planned path point to a desired pose, where the torch points directly at the cylindrical axis of the pipe and weld seam center, with a certain distance. To be specific, the welding torch path is a circle with the following properties: the distance to axis Z_w, the translation along axis Z_w, and the rotation around axes X_w and Y_w in the pipe frame are constants, while the rotation around axis Z_w is the only variable. In other words, the torch position along axes X_w, Y_w and Z_w and the rotation around axes X_w and Y_w in the pipe frame need to be optimized to achieve the aforementioned desired pose. To this end, a structured light-based visual servoing method is utilized in this paper.

C. WORKING PRINCIPLE

The working principle of visual servoing can be described by the following equation [34]:

$$\dot{e} = L_s V_c \tag{1}$$

where $\dot{e}$ is the time derivative of the error of the visual feature $e = s - s^*$; s and s^* are the current and desired visual features, respectively; L_s is the interaction matrix; and V_c is the camera velocities. Generally, the visual feature e is designed with

$$\dot{e} = -\lambda L_s \hat{L}_s^+ e, \tag{2}$$

where λ is a positive gain; $\hat{L}_s^+$ is the pseudoinverse of the approximation of the interaction matrix L_s. As long as $L_s\hat{L}_s^+$ is positive definite during the entire procedure, the stability of the control law is ensured. In other words, the robot will always move to the desired pose if s does not equal s^*.

This paper focuses on visual feature design and control law (interaction matrix) design. For visual feature design, the designed visual features should reflect the torch translation along axes X_w, Y_w and Z_w and rotation around axes X_w and Y_w; that is, the visual features can determine a circle on the cross section of a cylindrical surface, which can be represented by the phase map in the fringe projection method. Therefore, we will introduce the definitions of the fringe projection method and the phase map in subsection II-D. However, the phase map is composed of high-dimensional data. To speed up the computation and control, a low-dimensional cylindrical axis (constraining the torch translation along axes X_w and Y_w and rotation around axes X_w and Y_w) and the seam center (constraining the torch translation along axis Z_w) are expected to be extracted from the phase map. Therefore, the extraction algorithm is presented in section III. Extracted cylindrical axis and seam center are then utilized to design visual features for visual servo control, and the control law is deduced in section IV, where the stability of the control law is also proved.

The block diagram of the proposed structured light-based visual servoing method is shown in Fig.2. The fringe shifting patterns are projected onto the pipe's cylindrical surface, and the deformed patterns are captured and decoded to obtain the phase map. Then, the current visual feature s is extracted from the phase map. The difference between the desired visual feature s^* and current visual feature s^* is the input error of the control law; then, the expected camera velocity V_c is calculated. Further, the robot velocity can be obtained with the calibrated hand-eye transformation matrix ${}^eT_c$ to optimize the pose of the welding torch.

It is noted that the desired visual features s^* can be directly calculated by the camera and the projector model

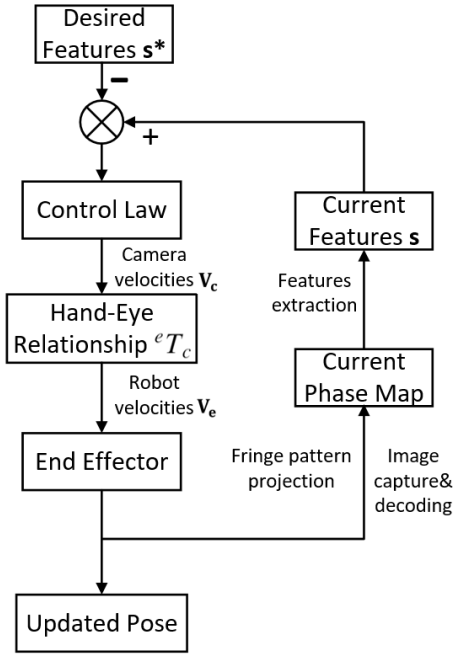

FIGURE 2. Block diagram of the proposed structured light-based visual servoing method.

using the desired torch pose ${}^{t}T_b$ and the accurately calibrated transformation matrices ${}^{t}T_e$, ${}^{e}T_b$ and ${}^{w}T_b$; the desired visual features s^* can also be determined when the welding torch is moved to the desired pose by other methods.

D. PHASE MAP DEFINITION AND GENERATION

The structured light method utilized in this work is called fringe projection method, which is defined as a method of using a digital video projector to project desired sinusoidal fringe patterns for phase retrieval [35]. For this method, a projector is used to project a series of phase-shifting sinusoidal stripe patterns, and a camera is used to capture deformed patterns synchronously. Then, by decoding, the so-called phase map is obtained, from which point cloud of the object's surface is reconstructed. The visual features for visual servoing are extracted from the phase map in this paper. Therefore, we introduce the phase map definition and generation in this section. The structured light-based visual servoing device consists of a projector and a camera, both of which are fixed on the robot end effector. Moreover, they are positioned purposely, with their optical axes being nearly parallel to each other, to reduce the complexity of feature extraction.

The model of the camera-projector rig with a cylinder at a random pose is shown in Fig. 3. Plane ABCD is the imaging plane of the camera, plane EFGH is the imaging plane of the projector, P is a random point that appears in both the camera and projector fields of view, and the corresponding pixel coordinates of the point in the camera image plane and projector image plane are (U_p, V_p) and (U_c, V_c), respectively. (u_p, v_p) and (u_c, v_c) are the corresponding normalized coordinates calculated by $(u_c, v_c, 1)^T = {M_c}^{-1}(U_c, V_c, 1)^T$ and

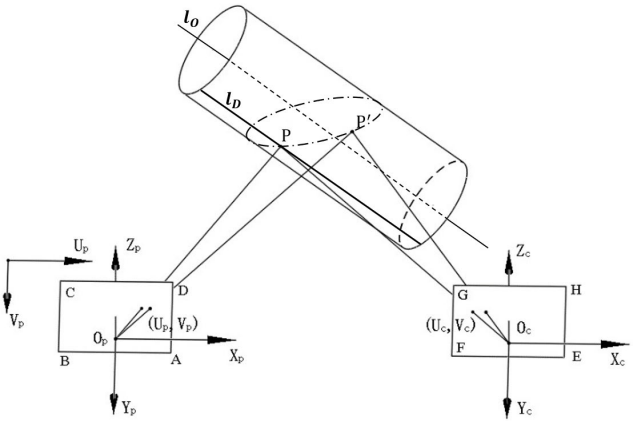

FIGURE 3. Model of the camera-projector rig.

$(u_p, v_p, 1)^T = {M_p}^{-1}(U_p, V_p, 1)^T$, where M_c and M_p are the intrinsic matrices of the camera and projector, respectively.

A phase map is defined as a matrix of the same size as the camera resolution. Each item of the phase map is the abscissa U_p in the projector image plane according to the corresponding camera pixel coordinate (U_c, V_c). Each item of the phase map is calculated from the variation in the intensity at each point of the image plane. First, a series of specific encoded sinusoidal fringe patterns with different phases are projected onto the pipes, and a sequence of corresponding images are captured by the camera. The value of a certain pixel with coordinate (U_p, V_p) in the fringe pattern is defined as

$$I_n^p(U_p, V_p) = A_n^p + B_n^p cos(2\pi f \phi(U_p, V_p) - 2\pi(n-1)/N), \tag{3}$$

where n is the phase shift index, I_n^p is the intensity of the pixel, A_n^p is the mean value, B_n^p is the amplitude, f is the frequency of the sinusoidal wave, and N is the total number of fringe patterns. Phase ϕ of pixel coordinate (U_c, V_c) in the camera image plane is then decoded using these images according to the formula

$$\phi(U_c, V_c) = \arctan \frac{-\sum_{n=1}^{N} I_n \sin[(2\pi/N)\cdot(n-1)]}{\sum_{n=1}^{N} I_n \cos[(2\pi/N)\cdot(n-1)]}, \tag{4}$$

where I_n is the intensity of a pixel at (U_c, V_c).

Then, those items considered to be the background according to the small fluctuation of the luminance are set to zero to reduce the amount of calculation.

To promote the accuracy and robustness, the dual-frequency phase shift method is utilized, in which unit-frequency sinusoidal fringe patterns are used to ascertain the general range of the phase, and high-frequency sinusoidal fringe patterns are used to ascertain the accurate value of the phase. The value U_p for the camera coordinate (U_c, V_c) is then calculated from the formula

$$U_p = ([((T_u/T_h)\cdot\phi_u - \phi_h)/2\pi - 0.5] + \phi_h/2\pi)\cdot T_h, \tag{5}$$

where T_u and T_h are the periods of the unit-frequency and high-frequency fringe patterns, ϕ_u and ϕ_h are the unit-frequency and high-frequency phases decoded from Eq. (4), and $[x]$ is the ceiling rounding operator that produces the minimum integer larger than x.

III. FEATURE EXTRACTION

Because the relative position between the camera and the welding torch remains unchanged, positioning the welding torch w.r.t two connecting pipes can be seen as positioning the camera in frame F_w. Therefore, how to represent the pose of the camera w.r.t the pipe is the prerequisite for motion control. To this end, the camera pose can be represented by the cylindrical axis (constraining the camera translation along axes X_w and Y_w and rotation around axes X_w and Y_w) and the seam center (constraining the camera translation along axis Z_w). One solution is to construct a 3D point cloud of the pipes, from which the cylindrical axis is extracted. However, 3D reconstruction is time consuming and induces calibration error. An alternative method is to extract the cylindrical axis and axial position from the phase map directly to speed up the computation. The axial position of the weld seam is easily determined by extracting the seam center in the phase map using an image processing algorithm. Therefore, this paper focuses on the extraction of the cylindrical axis. However, the cylindrical axis is not explicit in the phase map. Therefore, we first extract a characteristic generatrix on the cylindrical surface, which is parallel to the cylindrical axis, and then calculate the cylindrical axis using the characteristic generatrix by offsets along axes X_c and Z_c. Details of the extraction of the cylindrical axis are illustrated as follows.

A. EXTRACTION OF THE CHARACTERISTIC GENERATRIX

To extract the cylindrical axis from the phase map directly, the relationship of the phase map w.r.t the cylinder pose is studied. A cylinder at a random pose is shown in Fig. 3. Point P lies on the cylindrical surface. l_o is the cylindrical axis. l_D is the characteristic generatrix to be extracted and consists of the nearest point of every cross section of the cylinder, which is the plane with v_c determined by points P, O_p and O_c, where v_c is the normalized ordinate of P and O_p and O_c are the optical centers of the projector and camera, respectively, as shown in Fig. 4.

The intersection between this plane and the cylinder is an ellipse. The straight line MN represents the intersecting line between the normalized plane and the plane with a certain v_c. Therefore, the distance from MN to the line connecting the optical centers of the camera and projector O_cO_p is $d_1 = \sqrt{({v_c}^2+1)}$. The distance from P to line MN is d, so the distance from P to line O_cO_p is

$$d_1 + d = \sqrt{({v_c}^2+1)} + d. \tag{6}$$

According to the triangular similarity theorem, we have

$$u_p(u_c, v_c) - u_c = \frac{\sqrt{({v_c}^2+1)}}{\sqrt{({v_c}^2+1)}+d} \cdot L = Q(u_c, v_c), \tag{7}$$

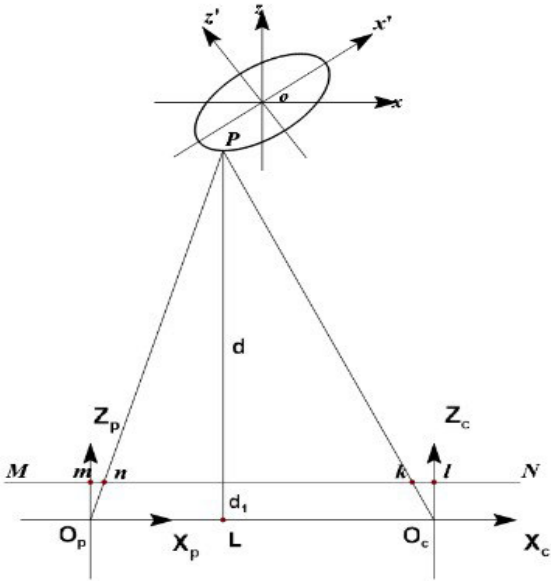

FIGURE 4. The ellipse is the intersection between the plane with a certain v_c and the cylinder.

where L is the length of O_cO_p. In Eq. (7), with constant L, it is not hard to derive that the larger $Q(u_c, v_c)$ is, the smaller d is.

For every v_c, which represents every row of matrix Q, the largest number is chosen, and the value $Q_{max}(v_c)$ and its position index $u_c(v_c)$ are recorded in an n-by-2 matrix $[Q_{max}(v_c), u_c(v_c)]$. The coordinate of a special point D, which is the intersection point of the characteristic generatrix and the plane with a certain v_c, can be derived as

$$\begin{cases} X_D = Z_D \cdot u_c \\ Y_D = Z_D \cdot v_c \\ Z_D = L/Q_{\max}. \end{cases} \tag{8}$$

Thus far, the 3D coordinate of point D in the camera coordinate frame has been derived, and for every v_c, there exists a unique point $D(v_c)$. Theoretically, all points $D(v_c)$ with different v_c lie on the same characteristic generatrix l_D, which is parallel to the central axis of the cylinder. With these points, the equation of line l_D can be acquired by least square fitting:

$$\begin{cases} x = \dfrac{u}{v}y + x_D \\ z = \dfrac{w}{v}y + z_D, \end{cases} \tag{9}$$

where (u, v, w) is the fitted direction vector of l_D and $(x_D, 0, z_D)$ is the intersection point of the straight line l_D and plane $y = 0$.

B. DERIVATION OF THE CYLINDRICAL AXIS

Since the cylindrical axis l_o is parallel to the characteristic generatrix l_D, only offsets along the X_c and Z_c axes, which are denoted as Δ_X and Δ_Z need to be ascertained to determine the equation of the axis l_o. Detailed procedures can be seen

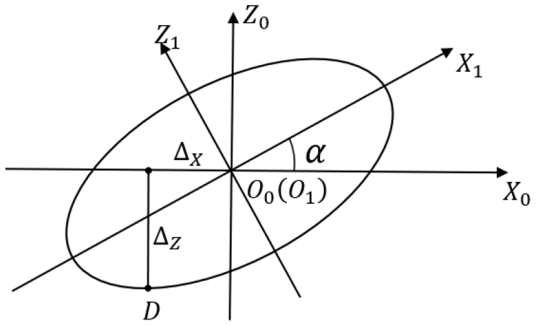

FIGURE 5. Coordinate frame F_0 translated from camera frame F_c, and F_1 rotated around Y_0 from F_0 by angle α. The ellipse is the intersection between plane X_1OZ_1 and the cylinder. The elliptical equation in F_1 is standard.

in Appendix A. Therefore, the coordinate of point O, which is the intersection point between the cylindrical axis l_o and the plane $y = 0$, can be calculated as

$$\begin{cases} x_o = x_D + \Delta_X = x_D + \dfrac{u'^2 + w'^2}{u'/w' + w'(u'^2 + 1 + w'^2)/u'} \\ \qquad \cdot R \cdot \sqrt{(w'^2 + 1)} \\ y_o = 0 \\ z_o = z_D + \Delta_Z = z_D + R \cdot \sqrt{(w'^2 + 1)}. \end{cases} \tag{10}$$

The entire deduction of the cylindrical axis l_o can be summarized as follows. First, a generatrix of cylinder l_D is extracted and fitted based on its geometrical characteristics. Then, the offsets of the cylindrical axis w.r.t the generatrix along the x and z axes are deduced and combined with the equation of l_D to produce the equation of l_o:

$$\begin{cases} x = \dfrac{u}{v} y + x_o \\ z = \dfrac{w}{v} y + z_o. \end{cases} \tag{11}$$

IV. CONTROL LAW

In this section, the extracted cylindrical axis and axial position of the weld seam are further utilized to design visual features for visual servoing. Then, the corresponding control law is derived, and the global asymptotic stability of this control law is demonstrated.

A. DERIVATION OF THE CONTROL LAW

To control the pose of a cylindrical axis in camera frame F_c, four degrees of freedom (DOFs) of the cylinder need to be constrained. They include translation along axes X_w and Z_w and rotation around axes X_w and Z_w. To this end, visual features are defined as two components of the direction vector of l_o and the coordinates of the intersection point between l_o and plane $X_cO_cZ_c$: $s = [x_o, z_o, u/v, w/v]^T$.

Through lengthy derivation (see Appendix B), the interaction matrix with 4 visual features can be obtained as:

$$L_s = \begin{bmatrix} -1 & u & 0 & -uz_o & -z_o & ux_o \\ 0 & w & -1 & -wz_o & x_o & wx_o \\ 0 & 0 & 0 & -uw & -w & 1+u^2 \\ 0 & 0 & 0 & -1-w^2 & u & ux_o \end{bmatrix}. \tag{12}$$

At this point, the pose of the cylindrical axis in the camera coordinate frame can be controlled to converge to the desired one, and the next step is to make the welding torch aim at the weld seam with such a pose. To this end, the weld seam is recognized by a geometrical method in the phase map, and the seam center (x^s, y^s, z^s) in camera frame F_c is calculated as the mean of all recognized seam points. A component of the coordinates of the seam center y^s is chosen as the fifth feature to constrain the translation along the cylindrical axis.

By combining Eq. (25) and Eq. (30), we obtain the interaction matrix with 5 visual features:

$$L_s = \begin{bmatrix} -1 & u & 0 & -uz_o & -z_o & ux_o \\ 0 & -1 & 0 & z^s & 0 & -x^s \\ 0 & w & -1 & -wz_o & x_o & wx_o \\ 0 & 0 & 0 & -uw & -w & 1+w^2 \\ 0 & 0 & 0 & -1-w^2 & u & uw \end{bmatrix}. \tag{13}$$

In the proposed method, because L_s at every iteration can be calculated by visual features s, we can directly choose $\hat{L}_s^+ = L_s^+$ in the control law $V_c = -\lambda \hat{L}_s^+ e$. Control schemes using $\hat{L}_s^+ = L_{s^*}^+$ and $\hat{L}_s^+ = 1/2(L_s + L_{s^*})^+$, where L_{s^*} is the interaction matrix at the desired pose, can also be chosen, and their performance comparison and discussion will be conducted in section V.

B. STABILITY ANALYSIS

As described above, it is obvious that the first, second, third and fourth rows of L_s are linearly independent of each other. Additionally, the first, second, third and fifth rows of L_s are linearly independent. To prove that all rows of L_s are linearly independent, we only have to prove the linear independence of the fourth and fifth rows of L_s. We can construct a matrix C as follows:

$$C = \begin{bmatrix} -uw & -w & 1+u^2 \\ -1-w^2 & u & uw \end{bmatrix}. \tag{14}$$

If $w = 0$, we have

$$C = \begin{bmatrix} 0 & 0 & 1+u^2 \\ -1 & u & 0 \end{bmatrix}. \tag{15}$$

This item $1 + u^2 \neq 0$ is ensured, which indicates $rank(C) = 2$.

If $w \neq 0$, using elementary row transformation, we obtain

$$C = \begin{bmatrix} -uw & -w & 1+u^2 \\ -1-u^2-w^2 & 0 & uw + u^3/w + u/w \end{bmatrix}. \tag{16}$$

The item $-1 - u^2 - w^2 \neq 0$, and the item $-w \neq 0$ will always be satisfied; thus,$rank(C)$ remains 2. The condition $rank(L_s) = 5$ is satisfied the entire time. Therefore,

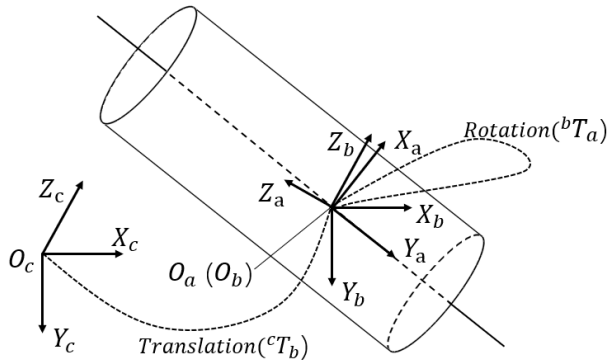

FIGURE 6. A cylinder at a random position in the camera coordinate frame F_c, in frame F_b, which is translated from F_c, and in F_a, where the axis of the cylinder coincides with O_aY_a and O_a lies on plane $X_cO_cZ_c$.

$Ker(L_sL_s^+) = \emptyset$, yielding that only one equilibrium point $e = 0$ exists. Furthermore, $L_sL_s^+$ equals a 5-by-5 identity matrix during the entire process, and the control law can be derived as

$$\dot{e} = -\lambda L_sL_s^+(s - s^*) = -\lambda(s - s^*), \tag{17}$$

which indicates that every feature will converge to the desired value at an exponential rate from any initial pose; i.e., global asymptotic stability of the proposed IBVS technique using $\hat{L}_s^+ = L_s^+$ is ensured.

V. SIMULATIONS

In the simulations, to simplify the modeling process, the welding joint of two pipes is ignored; hence, they can be seen as a whole cylinder. The phase map in the simulation is generated by straightforward solving of the equations of the intersection between straight lines and a cylinder. Each straight line represents an imaginary light ray that goes through a pixel on the image plane and the optical center of the camera, and the cylinder at the random pose is expressed as an equation in the camera coordinate frame.

The detailed procedure is shown as follows. In Fig. 6, the transformation from the camera coordinate frame to a special coordinate frame F_a is

$$\begin{aligned} &{}^aT_c \\ &= Rotx(-\alpha) \cdot Rotz(\gamma) \cdot Transl(-x_o, 0, -z_o) \\ &= \begin{bmatrix} \cos\gamma & -\sin\gamma & 0 & -x_o\cos\gamma \\ \cos\alpha\sin\gamma & \cos\alpha\cos\gamma & \sin\alpha & 0 \\ -\sin\alpha\sin\gamma & -\sin\alpha\cos\gamma & \cos\alpha & z_o sin\alpha\sin\gamma \\ 0 & 0 & 0 & 1 \end{bmatrix}, \end{aligned} \tag{18}$$

where $\sin\alpha = w$, $cos\alpha = \sqrt{u^2+v^2}$, $\sin\gamma = u/\sqrt{u^2+v^2}$ and $\cos\gamma = v/\sqrt{u^2+v^2}$. By injecting ${}^aP = {}^aT_c \cdot {}^cP$ into ${}^ax^2 + {}^az^2 = R^2$, we can obtain

$${}^cz = \frac{-(ab+cd) \pm \sqrt{(ab+cd)^2 - (a^2+c^2)(b^2+d^2-R_1^2)}}{a^2+c^2}, \tag{19}$$

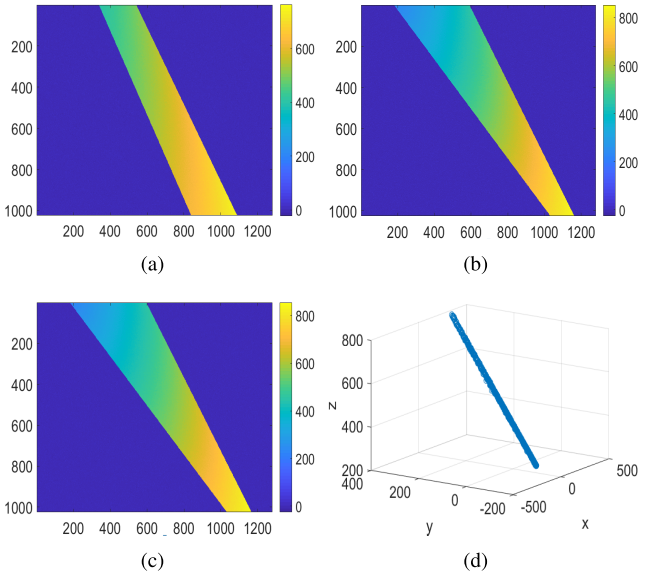

FIGURE 7. (a) Phase map at the initial pose. (b) Phase map at the end pose using $\hat{L}_s^{-1} = L_s^{-1}$. (c) Phase map at the desired pose. (d) Extracted axis.

where $a = vv_c - uu_c$, $b = -vx_o$, $c = uwv_c + vwu_c - (u^2+v^2)$, $d = -uwx_o + (u^2+v^2)z_o$, $R_1 = R\sqrt{u^2+v^2}$ and R is the radius of the cylinder. ${}^cz$ with smaller absolute value is chosen considering physical limits. Once ${}^cz$ is ascertained, the corresponding space point $({}^cx, {}^cy, {}^cz)$ for a pixel with the normalized coordinate (u_c, v_c) can be calculated by ${}^cx = {}^cz \cdot v_c$ and ${}^cy = {}^cz \cdot u_c$. The transformation between the camera and projector frame is E_3, which is a 3-by-3 unit matrix, and ${}^pt_c = \begin{bmatrix} 100 & 0 & 0 \end{bmatrix}^T$. Therefore, U_p for (u_c, v_c) is calculated by $U_p = ({}^cx + 100)f_{xp}/{}^cz + U_{op}$, where f_{xp} and U_{op} are the first and third items in the first row of projector intrinsic matrix M_p.

To compare the performance of visual servoing with different control schemes, simulations are conducted, and the results can be seen in Fig.8. All simulation experiments are performed with MATLAB of version 2017b. To prove the robustness of the proposed method, Gaussian noise with a variance of 1 is added to the phase map. To reduce the impact of noise, a mean filter is utilized in calculating Q_{max} and the u_c coordinate. The entire visual servoing simulation process works as follows. First, the desired visual features are set as $x^* = 50mm$, $z^* = 450mm$, $u^* = 0.8$ and $w^* = 1$, and the phase map at the desired pose is shown in Fig. 7(c). Second, the camera is moved to the initial pose, with the features being $x_1 = 30mm, z_1 = 500mm, u_1 = 0.5$ and $w_1 = -0.2$, and the phase map is shown in Fig. 7(a). Third, the phase map is calculated as explained above, from which the features are extracted and sent to the control law to move the camera to the next position. Having reached the next pose, the aforementioned procedures will be repeated until the cylinder converges to the desired pose. The termination criterion is $|e_w| < 0.01°$ as well as $|e_x| < 0.01mm$. In order to ensure the success of convergence and to present smooth and

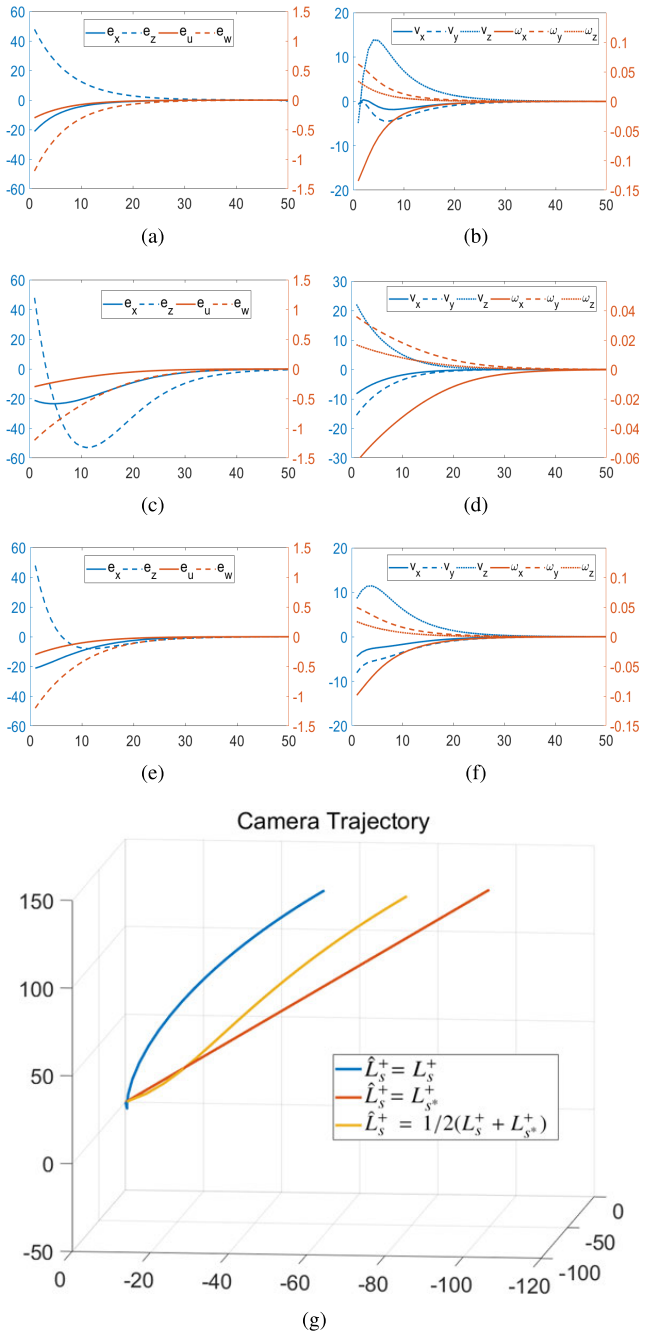

FIGURE 8. The first, second and third rows are results obtained using $\hat{L}_s^+ = L_s^+$, $\hat{L}_s^+ = L_{s^*}^+$, and $\hat{L}_s^+ = 1/2(L_s^+ + L_{s^*}^+)$, respectively. (a), (c), (e) Errors versus iterations (in number of times). (b), (d), (f) Camera velocities (in *mm*/*s* and *rad*/*s*) versus iterations (in number of times). (g) Camera trajectories using these three control schemes.

clear curves of errors, velocities and 3D camera trajectories of the three control schemes, the gain λ is set as 0.5, and the step time is 0.2 seconds.

The results show that when using $\hat{L}_s^+ = L_s^+$, errors converge asymptotically to zero, and the initial linear velocities of the camera are smaller than in the other two schemes. When using $\hat{L}_s^+ = L_s^+$ as the control scheme, asymptotic convergence of errors to zero is ensured: $e = -\lambda(s - s^*)$. When using $\hat{L}_s^+ = L_{s^*}^+$, linear and angular velocities converge to zero asymptotically, but error e_z decreases significantly to a large negative value at approximately the $15th$ iteration, which may cause a collision between the cylinder and camera or projector in real experiments. When using $\hat{L}_s^+ = 1/2(L_s^+ + L_{s^*}^+)$, errors converge faster to zero than in the other two schemes, and error e_Z converges much better than in the second control scheme. The camera trajectories are shown in Fig.8.(g). Because $\hat{L}_s^+$ remains unchanged when using $\hat{L}_s^+ = L_{s^*}^+$, the camera goes straight to the desired pose. It should be noted that the end poses obtained using these three schemes are all different from each other. The reason is that only 4 DOFs of the camera are constrained. Hence, both rotation around the cylindrical axis and translation along it will not induce variation of the phase map. Visual servoing simulations using these three schemes all converge to the desired pose. Both control schemes using $\hat{L}_s^+ = L_s^+$ and $\hat{L}_s^+ = L_{s^*}^+$ perform well in error convergence and camera trajectory. However, only the global asymptotic stability of the former scheme can be ensured. To ensure the success of the visual servoing process in real experiments, the control scheme using $\hat{L}_s^+ = L_s^+$ is used.

VI. EXPERIMENTS AND DISCUSSION

In order to demonstrate the feasibility of the proposed method, path planning using offline programming, teaching and this method are performed and compared. As mentioned previously, the entire visual servo system is composed of a projector (DLP Lightcrafter 4500) that projects fringe patterns, a camera (JAI GO-5000M-USB) that captures deformed fringe patterns, a weld torch, a computer with clock rate of 2.8 GHZ that decodes the fringe patterns to produce the phase map and calculates the robotic movement accordingly, and a robot manipulator (ABB IRB 1200) on which the camera, projector and weld torch are fixed. The projector and camera have resolutions of 912 × 1140 pixels and 2048 × 2560 pixels, respectively. The proposed method is also suitable for robots from other manufacturers, such as KUKA and Motoman, because the category of robot isn't relevant to this method. The visual servoing device in the real scenario is shown in Fig.9. The diameter and thickness of the two connecting steel pipes are 102*mm* and 4*mm*, respectively. Considering the thickness is less than 8*mm*, according to [36], a butt-weld joint with an I-groove is used for it's simple to prepare, economical to use and provides satisfactory strength, and the gap of it is approximately 2*mm*.

A. OFFLINE PROGRAMMING

The whole offline programming-based path planning works as follows. First of all, several important transformation matrices are calibrated. A laser tracker(Leica emScon Absolute Tracker (AT901 series)) is used to determine the transformation matrix between laser tracker frame and steel pipe frame ${}^{L}T_w$, and the transformation matrix between laser tracker frame and robot base frame ${}^{L}T_b$. ${}^{L}T_w$ is determined by following steps. First, measuring several points on the

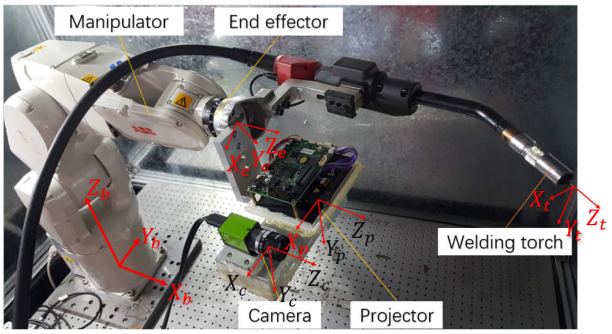

FIGURE 9. The camera-projector rig-based welding robot system.

right side of pipe and fitting a plane. Then, measuring the pipe and fitting the cylindrical axis. Afterwards, the origin of the pipe frame can be determined as the intersection point between this plane and axis. Y_w can also be obtained by orientation of the axis, with direction as shown in Fig.10 (a). By setting Z_w as vertical upward, ${}^{L}T_w$ can be obtained. The robot base frame is shown in Fig.9. By measuring the three plane and symmetric mounting holes of the subplate, ${}^{L}T_b$ can also be determined. ${}^{b}T_w$ can then be calculated as ${}^{L}T_b^{-1} \cdot {}^{L}T_w$. The transformation matrix ${}^{e}T_t$ can be calibrated by ABB 6 points calibration method. Path points are set as one of every 5 degrees. Planned torch pose at one path point is shown in Fig.10. Transformation matrix from planned torch pose at one path point to pipe frame ${}^{w}T_{t'}$ is then determined. Finally, transformation matrix is calculated as ${}^{b}T_e = {}^{b}T_w \cdot {}^{w}T_{t'} \cdot {}^{e}T_t{}^{-1}$, which can be used to calculate Euler angle and put to robot controller to move end effector to planned path point. At 9 different path points planned by offline programming, we measure and fit the axes of torch and the pipe, as shown in Fig.10 (c). Deviated distances and angles from the desired ones, which are 0*mm* and 90°, respectively, between axes of the torch and the pipe can be seen in Fig.15. The mean error and the root mean square error(RMSE) of distance and angle are directly calculaed as 1.1945*mm*, 1.2534*mm*, 1.0386° and 1.0712° respectively.

B. TEACHING

We also performed teaching experiments to analyze its accuracy. 10 path points are taught through FlexPendant by human visual guide and then memorized by robot controller. After that, the manipulator will move to each path point, where we measure and fit the axis of torch. Deviated distances and angles from the desired ones (0*mm* and 90°, respectively) between axes of the torch and the pipe by teaching can be seen in Fig.11 (b). The mean error and RMSE of distance and angle are directly calculated as 8.3093*mm*, 10.3514*mm*, 1.8337° and 2.2965° respectively.

C. THE PROPOSED METHOD

First, the intrinsic and extrinsic parameters of the projector and the camera are calibrated according to [37]. Second, to accurately control the camera, the transformation matrix

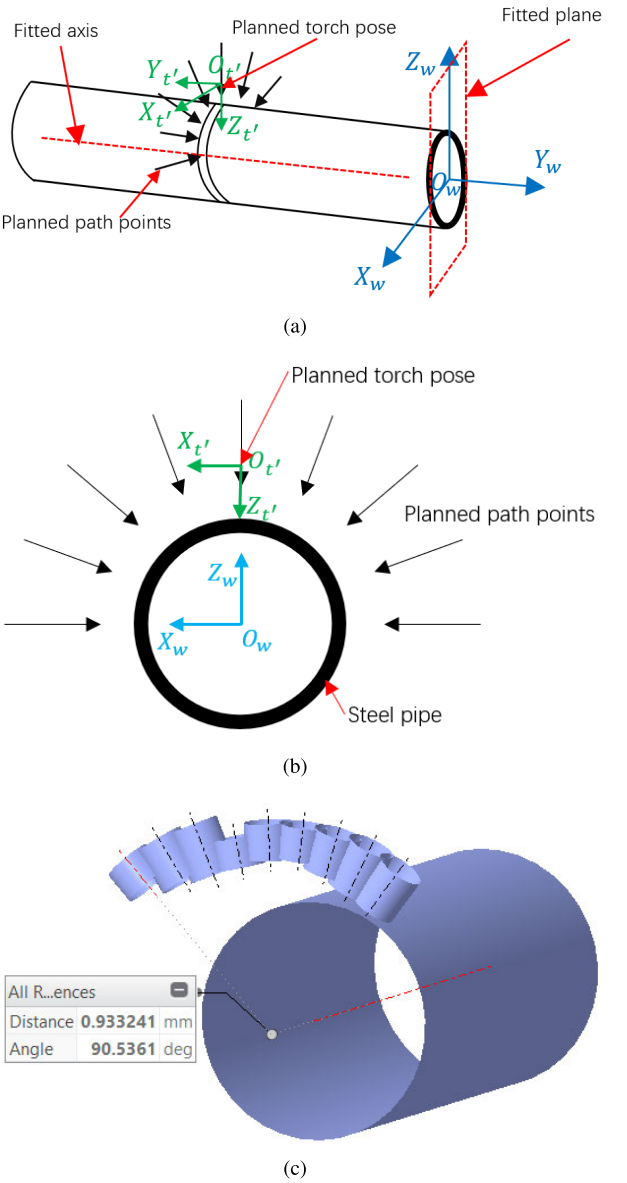

FIGURE 10. General view (a) and lateral view (b) of the steep pipe. Black arrows represent a series of planned path points. Green coordinate frame represents the torch pose. Note only torch pose at one path point is shown, while others are omitted for their similarity. (c) Measured and fitted cylinders of the pipe and the torch at different poses by offline programming.

between the end effector frame and camera frame ${}^{e}T_c$ is ascertained by hand-eye calibration [38]. The transformation matrix ${}^{t}T_e$ is calibrated by the *ABB* 6 points TCP calibration method. ${}^{w}T_b$ is calibrated by method mentioned in VI-A. The step number N of the dual-frequency phase shift method is set to 20. The transformation matrices ${}^{t}T_e$ and ${}^{w}T_b$ are both roughly calibrated, so visual features at the desired pose cannot be determined directly and accurately from these matrices. At the beginning of the experiment, the robot end effector is moved to the desired pose based on deviations measured by the laser tracker and transformation matrices ${}^{t}T_e$, ${}^{e}T_b$ and ${}^{w}T_b$. Then, the phase map at the desired pose is

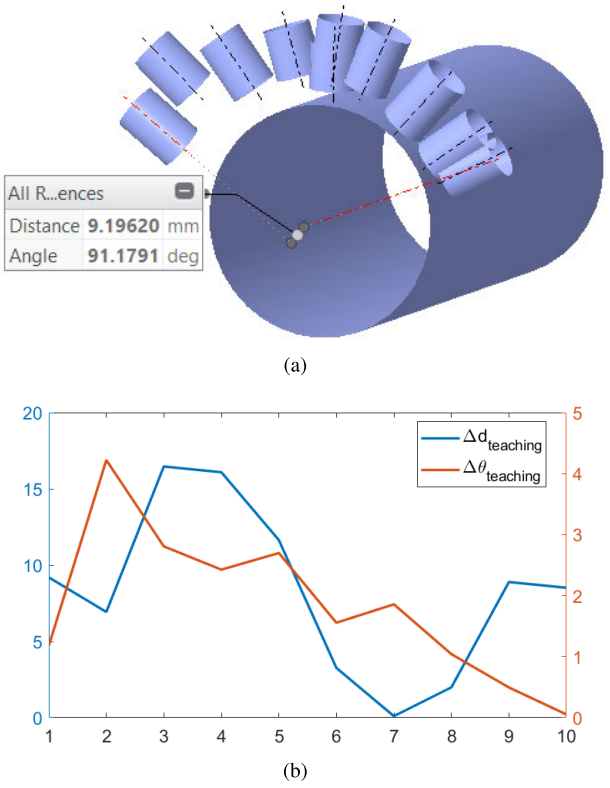

FIGURE 11. (a) Measured and fitted cylinders of the pipe and the torch at different poses by teaching. (b) Deviated distances (in *mm*) and angles (in °) between axes of the torch and the pipe by teaching.

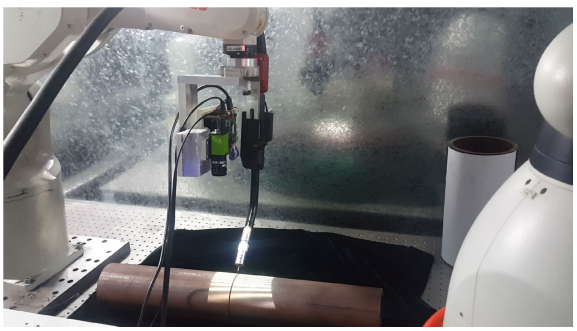

FIGURE 12. The camera-projector rig-based welding system in a real scenario.

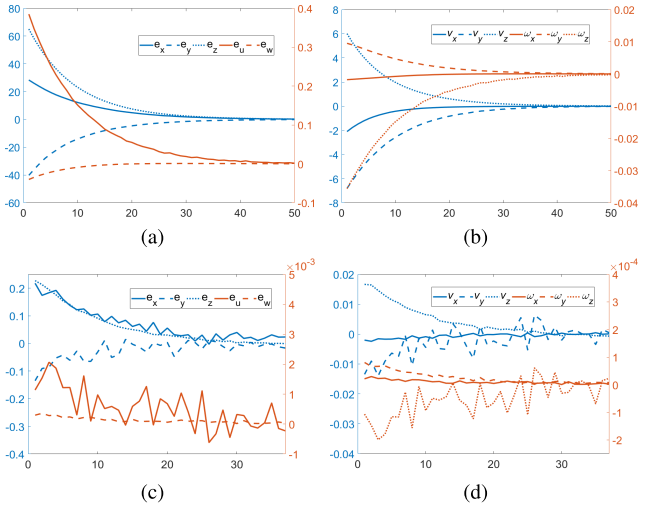

FIGURE 13. The first and second rows are experimental results at the far and near initial poses, respectively. (a), (c) Errors versus iterations (in number of times). (b), (d) Camera velocities (in *mm*/*s* and *rad*/*s*) versus iterations (in number of times).

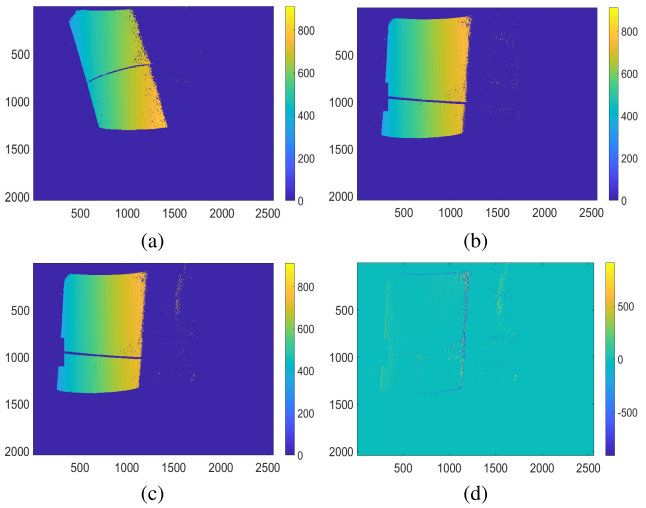

FIGURE 14. (a) Phase map at the initial pose far from the desired position. (b) Phase map at the end pose. (c) Phase map at the desired pose. (d) Difference between phase maps at the end and desired poses.

generated, from which the desired features s^* are extracted. The control scheme using $\hat{L}_s^+ = L_s^+$ is chosen. The proposed visual servoing method is image-based, so calibration errors of the camera-projector rig and the hand-eye relationship will not affect its final accuracy. The visual servoing process works as follows:

1) The projector projects fringe patterns, and the camera captures images with deformed fringe patterns, from which the computer produces the phase map and extracts the current features.

2) If the current features are within the allowable range, then the iteration ends; if not, the current features will be substituted into the control law to produce camera movement.

3) The robot end effector moves according to the calculated camera movement and hand-eye relationship.

4) Go back to step 1).

In order to demonstrate the effectiveness of the proposed method, experiments with both far and near initial poses are conducted, and the error curves and velocities curves are shown in Fig.13. Phase maps at different poses in one experiment, where the initial pose is far from the desired one, are shown in Fig.14. Moreover, to prove the accuracy of this method, 9 extra experiments are performed, in which the robot end effector is moved to 9 different far initial poses. In each experiment, the deviated distance and angle from the desired ones(0mm and 90°, respectively) between the axes of the torch and the pipe are accurately measured by the

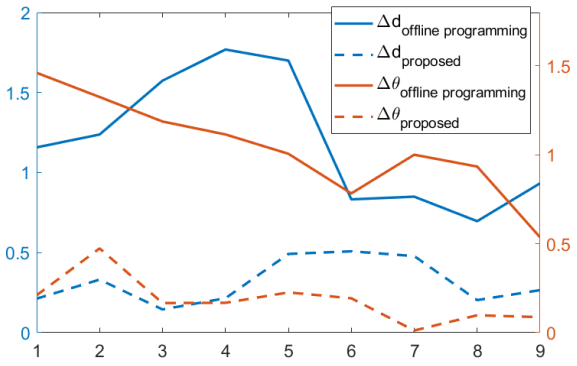

FIGURE 15. Deviated distances (in *mm*) and angles (in °) between axes of the torch and the pipe by offline programming and the proposed method.

TABLE 1. Chemical components of AISI 1020 steel.

Element	Mn	C	S	P	Fe
w%	0.30-0.60	0.18-0.23	<0.05	<0.04	Bal

TABLE 2. Welding parameters of GMAW.

Parameter	Value
Current	100A
Voltage	17V
Travel speed	4*mm*
Nozzle-to-work distance	18*mm*
Shielding gas	80%Ar+20%CO_2
Shielding gas flow rate	15L/min

laser tracker. Results are shown in Fig.15. The mean error and RMSE of distance and angle are directly calculated as 0.3169*mm*, 0.3438*mm*, 0.1818° and 0.2187° respectively.

D. WELDING EXPERIMENTS

In order to compare the three methods further, welding experiments were also conducted. Gas metal arc welding (GMAW) is chosen for its versatility, speed and the relative ease of adapting to the process to robotic automation. All welding experiments were performed on a MIG/MAG welding machine (Panasonic YD-350GL4), and filler wire (ER70S-6) of 1.0*mm* diameter with copper coated was used. The steel type of steel pipes is AISI 1020, the chemical composition of which is shown in Table 1. This type of steel is widely applied to manufacture axles, general engineering and machinery parts and components, spindles and so on. Welding parameters include welding current, voltage, torch travel speed, and nozzle-to-work distance among others. Their values are shown in Table 2. Results using teaching, offline programming and the proposed method are shown in Fig. 16.

E. DISCUSSION

As shown in Fig.14, the difference between the phase maps at the end and desired poses is small, which indicates that the torch tip-to-seam center deviation is small. It should

FIGURE 16. Welding results using (a) teaching, (b) offline programming, and (c) the proposed method. Both welds and heat affected zone (HAZ) are more well-distributed when using the proposed method. The shinny areas are not pores, and they appears when attached copper is removed.

be noted that substantial noise exists around the edge of pipes in a phase map, partly because those pixels with low illumination variation are assumed to be background and directly set to zero. However, feature extraction was barely influenced because only values around the maximum of every row, i.e., near the center of the pipe, but not all of them, are considered in the axis feature extraction. Hence no image filtering method is required, which ensures the high accuracy of cylindrical axis extraction.

Experiments with both far and near initial poses are conducted, and the results are shown in Fig.13. Errors and velocities all converge to zero for either the far or near initial pose, which means that the proposed method is feasible. Moreover, in Fig.13 (c), the error fluctuation between two consecutive iterations is rather small, which indicates that the proposed novel feature extraction method is robust to noise. It should be noted that when using the same control scheme $\hat{L}_s^+ = L_s^+$, although error curves in the simulation and in the real experiment both converge to zero exponentially, their velocity curves exhibit different behaviors, as shown in Fig. 8 (a, b) and Fig. 13 (a, b). The exponential convergence of camera velocities is not ensured when using the control scheme $\hat{L}_s^+ = L_s^+$. However, when initial errors e_x and e_z are positive, both camera velocities and errors converge to zero exponentially.

Comparing the three method, it is obvious that the proposed method is superior than the other two in accuracy, as shown in Fig.11, Fig.15. Results show this method can improve the mean error of distance and angle of offline programming by 73.5% and 82.5%. Thus this method can improve the accuracy of offline programming. In Fig.16, both welds and heat affected zone (HAZ) are more well-distributed when using the proposed method. The remaining error may be induced by hand-eye calibration error, TCP calibration error, pipe surface roughness, measurement and fitting error and so on. These factors will be considered, and achieving more accurate positioning tasks will be studied in the years to come.

VII. CONCLUSION

To guarantee the welding quality of robotic pipe welding, the welding torch needs to point directly at the axis of the

pipe during the entire welding procedure. To adjust the pose of the welding torch at each path point planned by offline programming, a structured light-based visual servoing method is proposed. In this method, fringe projection is utilized to address the problem of a texture-less pipe surface. The visual servoing is used to position the welding torch in the desired pose based on a phase map. A low-dimensional cylindrical axis is extracted directly from a high-dimensional phase map to represent the pipes' cylindrical surface, and the seam center is also extracted to represent the axial position of the weld seam, resulting in faster computation. A control law based on the extracted cylindrical axis and seam center is constructed, and its global asymptotic stability is proved. The proposed method can optimize the accuracy of offline programming for two reasons. First, the influences of the installation error, modeling error and part deformation will be excluded after visual servoing. Second, because every pose of the torch is truly reached and memorized by the robotic controller, the high repeat positioning accuracy of industrial robots is fully utilized. Simulations and real experiments show that features converge to the desired ones at a nearly exponential rate, and velocities of the camera all converge to zero even when substantial noise exists and the initial pose is far from the desired one, which verifies the feasibility and robustness of this method. In experiments, after adjustment, the deviations between the axes of the pipe and the welding torch are small, which demonstrates the accuracy of this method. Welding experiments also show that this method can produce more well-distributed welds and HAZ.

Methods for accelerating phase map generation and robotic movement calculation will be studied in future studies. The positioning task w.r.t an object with a more complex and general texture-less surface, including a quadratic surface and a free-form surface, will also be considered in the future.

APPENDIX A
DETAILED DERIVATION OF THE OFFSETS BETWEEN THE CHARACTERISTIC GENERATIX AND THE CYLINDRICAL AXIS

The offsets along the X_c and Z_c axes are denoted Δ_X and Δ_Z, as shown in Fig. 5. Δ_Z can be deduced as $\Delta_Z = R/\sin\beta$, where R is the radius of the cylinder, and $\beta = \arcsin(v/\sqrt{(w^2+v^2)})$, in which (u, v, w) is the direction vector of l_D. For the sake of clarity and simplicity, the direction vector of l_D is set as $(u', 1, w')$, where $u' = u/v$ and $w' = w/v$. This is feasible because the circumstance in which v equals zero is rare and will never appear in our applications. Therefore, Δ_Z can also be denoted as

$$\Delta_Z = R/\sin\beta = R\cdot\sqrt{(w'^2+1)}. \tag{20}$$

The relationship between Δ_X and Δ_Z is deduced as follows. As shown in Fig. 5, the equation of the ellipse in coordinate frame $X_1\ OZ_1$ is ${x_1}^2/a^2 + {z_1}^2/b^2 = 1$, where $a = R/\cos\gamma, \cos\gamma = 1/\sqrt{u'^2+1+w'^2}$, and $b = R$ because the ellipse can be considered as the intersection of plane $X_1O_1Z_1$ with a cylinder that is rotated around axis OZ_1 by a certain angle γ. The transformation from coordinate frame $X_0\ OZ_0$ to $X_1\ OZ_1$ is

$$\begin{bmatrix} x_1 \\ z_1 \end{bmatrix} = \begin{bmatrix} \cos\alpha & \sin\alpha \\ -\sin\alpha & \cos\alpha \end{bmatrix} \cdot \begin{bmatrix} x_0 \\ z_0 \end{bmatrix}. \tag{21}$$

By combining the above equations, we derive the elliptical equation in the coordinate frame $X_0\ OZ_0$:

$$(x_0\cos\alpha + z_0\sin\alpha)^2\cos^2\gamma + (x_0\sin\alpha + z_0\cos\alpha)^2 = R^2. \tag{22}$$

By differentiating Eq. (22) and letting $dz_0/dx_0 = 0$, we obtain the relationship between Δ_X and Δ_Z:

$$\Delta_X = \frac{\sin^2\gamma\cdot\tan\alpha}{\cos^2\gamma + \tan^2\alpha}\cdot\Delta_Z, \tag{23}$$

where $\sin\gamma = \sqrt{u'^2+w'^2}/\sqrt{u'^2+1+w'^2}$, and $\tan\alpha = w'/u' = w/u$.

Eq. (23) can also be simplified as

$$\Delta_X = \frac{u'^2+w'^2}{u'/w' + w'(u'^2+1+w'^2)/u'}\cdot\Delta_Z. \tag{24}$$

APPENDIX B
DETAILED DERIVATION OF THE INTERACTION MATRIX

Here, the well-known equation regarding how the differential motion of a camera induces the coordinate variation of a static point $P(x, y, z)$ is presented:

$$\begin{bmatrix} \Delta x \\ \Delta y \\ \Delta z \end{bmatrix} = \begin{bmatrix} -1 & 0 & 0 & 0 & -z & y \\ 0 & -1 & 0 & z & 0 & -x \\ 0 & 0 & -1 & -y & x & 0 \end{bmatrix} \cdot \begin{bmatrix} \delta x \\ \delta y \\ \delta z \\ \delta\theta_x \\ \delta\theta_y \\ \delta\theta_z \end{bmatrix}, \tag{25}$$

where Δx, Δy and Δz represent the coordinate variation of point P along the x, y and z axes, respectively; δx, δy, δz, $\delta\theta_x$, $\delta\theta_y$ and $\delta\theta_z$ represent the translational and rotational components of the camera differential motion.

Consequently, the equation regarding the variation of a spatial vector (u, v, w) caused by camera differential motion can be deduced:

$$\begin{bmatrix} \Delta u \\ \Delta v \\ \Delta w \end{bmatrix} = \begin{bmatrix} 0 & -w & -v \\ w & 0 & -u \\ v & u & 0 \end{bmatrix} \cdot \begin{bmatrix} \delta\theta_x \\ \delta\theta_y \\ \delta\theta_z \end{bmatrix}, \tag{26}$$

where $(\Delta u, \Delta v, \Delta w)$ denotes the variation of the spatial vector, and (u, v, w) is the direction vector before the camera was moved.

The equation of a straight line in the camera coordinate system before camera movement can be derived as

$$\frac{x-x_o}{u} = \frac{y-y_o}{v} = \frac{z-z_o}{w}. \tag{27}$$

To ascertain the intersection between this line and plane XOZ in the new camera coordinate frame, we let $y = 0$; by ignoring the variation of (u, v, w) due to its minuteness, we obtain

$$\begin{bmatrix} \Delta x_o \\ \Delta z_o \end{bmatrix} = \begin{bmatrix} -1 & u/v & o & -uz_o/v & -z_o & ux_o/v \\ 0 & w/v & -1 & -wz_o/v & x_o & wx_o/v \end{bmatrix} \cdot \begin{bmatrix} \delta x \\ \delta y \\ \delta z \\ \delta\theta_x \\ \delta\theta_y \\ \delta\theta_z \end{bmatrix}. \quad (28)$$

The relationship between the derivatives of k_x and k_z and the derivatives of u, v and w is obtained as

$$\begin{bmatrix} \dot{k}_x \\ \dot{k}_z \end{bmatrix} = \begin{bmatrix} 1/v & -u/v^2 & 0 \\ 0 & -w/v^2 & 1/v \end{bmatrix} \cdot \begin{bmatrix} \dot{u} \\ \dot{v} \\ \dot{w} \end{bmatrix}. \quad (29)$$

By combining Eq. (26), Eq. (28), and Eq. (29) and substituting $v = 1$, we obtain the interaction matrix with 4 visual features:

$$L_s = \begin{bmatrix} -1 & u & 0 & -uz_o & -z_o & ux_o \\ 0 & w & -1 & -wz_o & x_o & wx_o \\ 0 & 0 & 0 & -uw & -w & 1+u^2 \\ 0 & 0 & 0 & -1-w^2 & u & ux_o \end{bmatrix}. \quad (30)$$

ACKNOWLEDGMENT

The authors would like to thank the anonymous reviewers for their helpful suggestions and queries that helped to improve this paper.

REFERENCES

[1] M. Hemmatzadeh, H. Moshayedi, and I. Sattari-Far, "Influence of heat input and radius to pipe thickness ratio on the residual stresses in circumferential arc welded pipes of API X46 steels," *Int. J. Pressure Vessels Piping*, vol. 150, pp. 62–71, Feb. 2017.

[2] D. Yapp and S. A. Blackman, "Recent developments in high productivity pipeline welding," *J. Brazilian Soc. Mech. Sci. Eng.*, vol. 26, no. 1, pp. 89–97, 2004.

[3] H.-S. Moon, S.-H. Ko, and J.-C. Kim, "Automatic seam tracking in pipeline welding with narrow groove," *Int. J. Adv. Manuf. Technol.*, vol. 41, pp. 234–241, Mar. 2009.

[4] K.-Y. Bae, T.-H. Lee , and K.-C. Ahn, "An optical sensing system for seam tracking and weld pool control in gas metal arc welding of steel pipe," *J. Mater. Process. Technol.*, vol. 120, nos. 1–3, pp. 458–465, 2002.

[5] T. Yao, Y. Gai, and H. Liu, "Development of a robot system for pipe welding," in *Proc. Int. Conf. Measuring Technol. Mechatronics Automat.*, Mar. 2010, pp. 1109–1112.

[6] Y. Xu, H. Yu, J. Zhong, T. Lin, and S. Chen, "Real-time seam tracking control technology during welding robot GTAW process based on passive vision sensor," *J. Mater. Process. Technol.*, vol. 212, no. 8, pp. 1654–1662, Aug. 2012.

[7] W. J. Shao, Y. Huang, and Y. Zhang, "A novel weld seam detection method for space weld seam of narrow butt joint in laser welding," *Optics Laser Technol.*, vol. 99, pp. 39–51, Feb. 2018.

[8] H.-Y. Shen, J. Wu, T. Lin, and S.-B. Chen, "Arc welding robot system with seam tracking and weld pool control based on passive vision," *Int. J. Adv. Manuf. Technol.*, vol. 39, pp. 669–678, Nov. 2008.

[9] P. Rodríguez-Gonzálvez and M. Rodríguez-Martín, "Weld bead detection based on 3D geometric features and machine learning approaches," *IEEE Access*, vol. 7, pp. 14714–14727, 2019.

[10] C. Jiang, F. Zhang, and Z. Wang, "Image processing of aluminum alloy weld pool for robotic VPPAW based on visual sensing," *IEEE Access*, vol. 5, pp. 21567–21573, 2017.

[11] C. Z. Shuyan and S. Yonglun, "Models of weld pose and welding gun pose," *Chin. J. Mech. Eng.*, vol. 39, no. 7, pp. 59–62, 2003.

[12] J. Tian, M. Gao, and Y. He, "Intelligent control of welding gun pose for pipeline welding robot based on improved radial basis function network and expert system," *Int. J. Adv. Robotic Syst.*, vol. 10, no. 2, p. 115, Feb. 2013.

[13] X. Chen and J. Yu, "Acquisition and optimization of weld trajectory and pose information for robot welding of spatial corrugated Web sheet based on laser sensing," *Int. J. Adv. Manuf. Technol.*, vol. 96, nos. 9–12, pp. 3033–3041, 2018.

[14] M. A. Funes-Lora, E. A. Portilla-Flores, E. Vega-Alvarado, R. R. Blas, E. A. M. Cruz, and M. F. C. Romero, "A novel mesh following technique based on a non-approximant surface reconstruction for industrial robotic path generation," *IEEE Access*, vol. 7, pp. 22807–22817, 2019.

[15] Z. Pan, J. Polden, N. Larkin, S. van Duin, and J. Norrish, "Automated offline programming for robotic welding system with high degree of freedoms," in *Advances in Computer, Communication, Control and Automation*, vol. 121. Berlin, Germany: Springer, 2011, pp. 685–692.

[16] J. N. Pires, T. Godinho, and P. Ferreira, "CAD interface for automatic robot welding programming," *Ind. Robot*, vol. 31, no. 1, p. 716, 2004.

[17] T. Yifei, Z. Meng, L. Jingwei, L. Dongbo, and W. Yulin, "Research on intelligent welding robot path optimization based on GA and PSO algorithms," *IEEE Access*, vol. 6, pp. 65397–65404, 2018.

[18] L. Yang, E. Li, T. Long, J. Fan, and Z. Liang, "A novel 3-D path extraction method for arc welding robot based on stereo structured light sensor," *IEEE Sensors J.*, vol. 19, no. 2, pp. 763–773, Jan. 2019.

[19] P. Maiolino, R. Woolley, D. Branson, P. Benardos, A. Popov, and S. Ratchev, "Flexible robot sealant dispensing cell using RGB-D sensor and off-line programming," *Robot. Comput.-Integr. Manuf.*, vol. 48, pp. 188–195, Dec. 2017.

[20] F. Chaumette and S. Hutchinson, "Visual servo control. I. Basic approaches," *IEEE Robot. Autom. Mag.*, vol. 13, no. 4, pp. 82–90, Dec. 2006.

[21] J. Gao, G. Zhang, P. Wu, X. Zhao, T. Wang, and W. Yan, "Model predictive visual servoing of fully-actuated underwater vehicles with a sliding mode disturbance observer," *IEEE Access*, vol. 7, pp. 25516–25526, 2019.

[22] O. Tahri and F. Chaumette, "Point-based and region-based image moments for visual servoing of planar objects," *IEEE Trans. Robot.*, vol. 21, no. 6, pp. 1116–1127, Dec. 2005.

[23] L. Yang, Z. Liu, X. Wang, and Y. Xu, "An optimized image-based visual servo control for fixed-wing unmanned aerial vehicle target tracking with fixed camera," *IEEE Access*, vol. 7, pp. 68455–68468, 2019.

[24] B. Thuilot, P. Martinet, L. Cordesses, and J. Gallice, "Position based visual servoing: Keeping the object in the field of vision," in *Proc. IEEE Int. Conf. Robot. Automat.*, May 2002, pp. 1624–1629.

[25] V. Lippiello, J. Cacace, A. Santamaria-Navarro, J. Andrade-Cetto, M. Trujillo, Y. R. Esteves, and A. Viguria, "Hybrid visual servoing with hierarchical task composition for aerial manipulation," *IEEE Robot. Autom. Lett.*, vol. 1, no. 1, pp. 259–266, Jan. 2016.

[26] F. Yan, B. Li, W. Shi, and D. Wang, "Hybrid visual servo trajectory tracking of wheeled mobile robots," *IEEE Access*, vol. 6, pp. 24291–24298, 2018.

[27] J. Pages, C. Collewet, F. Chaumette, and J. Salvi, "Optimizing plane-to-plane positioning tasks by image-based visual servoing and structured light," *IEEE Trans. Robot.*, vol. 22, no. 5, pp. 1000–1010, Oct. 2006.

[28] W.-F. Xie, Z. Li, X.-W. Tu, and C. Perron, "Switching control of image-based visual servoing with laser pointer in robotic manufacturing systems," *IEEE Trans. Ind. Electron.*, vol. 56, no. 2, pp. 520–529, Feb. 2009.

[29] H. Sheng, J. Xu, K. Chen, and G. Zhang, "Visual servoing based on geometric features by surface structured light," in *Proc. IEEE 7th Annu. Int. Conf. CYBER Technol. Automat., Control, Intell. Syst. (CYBER)*, Jul./Aug. 2017, pp. 57–61.

[30] J. Xu, G. Rao, and Z. Chen, "Robotic visual servoing using fringe projection profilometry," *Proc. SPIE*, vol. 10819, Nov. 2018, Art. no. 108190Q.

[31] R. Chen, G. Wang, J. Zhao, J. Xu, and K. Chen, "Fringe pattern based plane-to-plane visual servoing for robotic spray path planning," *IEEE/ASME Trans. Mechatronics*, vol. 23, no. 3, pp. 1083–1091, Jun. 2018.

[32] C. Reich, R. Ritter, and J. Thesing, "3-D shape measurement of complex objects by combining photogrammetry and fringe projection," *Opt. Eng.*, vol. 39, no. 1, pp. 259–266, Jan. 2016.
[33] Q. Guo, J. Xi, L. Song, Y. S. Yu, Y. Yin, and X. Peng, "Fringe pattern analysis with message passing based expectation maximization for fringe projection profilometry," *IEEE Access*, vol. 4, pp. 4310–4320, 2016.
[34] W. Pan, M. Lyu, K. Hwang, M. Ju, and H. Shi, "A neuro-fuzzy visual servoing controller for an articulated manipulator," *IEEE Access*, vol. 6, pp. 3346–3357, 2018.
[35] S. Zhang, "High-speed 3D shape measurement with structured light methods: A review," *Opt. Lasers Eng.*, vol. 106, pp. 119–131, Jul. 2018.
[36] *Welding and Allied Processes—Recommendations for Joint Preparation—Part 1: Manual Metal-Arc Welding, Gas-Shielded Metal-Arc Welding, Gas Welding, TIG Welding and Beam Welding of Steels*, Standard ISO 9692-1:2003, 2003.
[37] R. Chen, J. Xu, H. Chen, J. Su, Z. Zhang, and K. Chen, "Accurate calibration method for camera and projector in fringe patterns measurement system," *Appl. Opt.*, vol. 55, no. 16, pp. 4293–4300, 2016.
[38] R. Y. Tsai and R. K. Lenz, "A new technique for fully autonomous and efficient 3D robotics hand/eye calibration," *IEEE Trans. Robot. Autom.*, vol. 5, no. 3, pp. 345–358, Jun. 1989.

JINQUAN LI received the B.E. degree in mechanical engineering from the Shaanxi University of Science and Technology, Xi'an, China, in 1992, and the Ph.D. degree in mechanical engineering from the Beijing Institute of Technology, Beijing, China, in 2004. He was a Postdoctoral Researcher with the Department of Precision Instrument and Mechanology, Tsinghua University, Beijing. He is currently an Associate Professor with the School of Automation, Beijing University of Posts and Telecommunications, Beijing. His research interests include intelligent equipment design, image processing, and fea method.

ZHE CHEN received the B.E. degree in mechanical engineering from China Agriculture University, Beijing, China. He is currently pursuing the master's degree in mechanical engineering with the school of Automation, Beijing University of Posts and Telecommunications, Beijing. He has been a Visiting Student with the Department of Mechanical Engineering, Tsinghua University, Beijing, since 2018. His research interests include machine vision, visual servo control, and intelligent robotics.

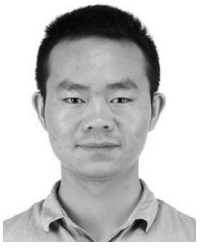

GANG RAO received the B.E. degree in mechanical engineering from Xi'an Jiaotong University, Xi'an, China, in 2014. He is currently pursuing the Ph.D. degree with the Department of Mechanical Engineering, Tsinghua University, Beijing, China. His research interests include manufacturing automation, 3-D measurement, and intelligent robotics.

JING XU received the Ph.D. degree in mechanical engineering from Tsinghua University, Beijing, China. He was a Postdoctoral Researcher with the Department of Electrical and Computer Engineering, Michigan State University, East Lansing, MI, USA.

He is currently an Associate Professor with the Department of Mechanical Engineering, Tsinghua University. His research interests include vision-guided manufacturing, image processing, and intelligent robotics.